metals

MDPI

Article

Powder Metallurgy Fabrication and Characterization of Ti6Al4V/xCu Alloys for Biomedical Applications

Hector Javier Vergara-Hernández [1,*], Luis Olmos [2], Victor Manuel Solorio [1], Didier Bouvard [3], Julio Villalobos-Brito [1], Jorge Chávez [4] and Omar Jimenez [5]

[1] División de Estudios de Posgrado e Investigación, Tecnológico Nacional de México/I.T. Morelia, Av. Tecnológico #1500, Colonia Lomas de Santiaguito, Morelia 58120, Mexico; d12121802@morelia.tecnm.mx (V.M.S.); julio.vb@morelia.tecnm.mx (J.V.-B.)
[2] Instituto de Investigaciones en Ciencias de la Tierra (INICIT), Universidad Michoacana de San Nicolás de Hidalgo, Fco. J. Mujica S/N, Morelia 58060, Mexico; luis.olmos@umich.mx
[3] National Centre for Scientific Research (CNRS), Science et Ingénierie des Matériaux et Procédés (SIMAP), Grenoble Institute of Technology (Grenoble INP), Universite Grenoble Alpes, 38000 Grenoble, France; didier.bouvard@grenoble-inp.fr
[4] Departamento de Ingeniería Mecánica Eléctrica, Centro Universitario de Ciencias Exactas e Ingenierías (CUCEI), Universidad de Guadalajara, Blvd. Marcelino García Barragán #1421, Guadalajara 44430, Mexico
[5] Departamento de Ingeniería de Proyectos, Universidad de Guadalajara, José Guadalupe Zuno #48, Los Belenes, Zapopan 45100, Mexico
* Correspondence: hector.vh@morelia.tecnm.mx

Abstract: Ti6Al4V (Ti64) alloy is the most used metal material for bone implants because of its good biocompatibility and adapted mechanical properties. Nevertheless, it shows low antibacterial activity, which may favor its failure. Addition of antibacterial elements such as copper should avoid this drawback. This work studies the addition of Cu into a Ti64 matrix resulting in Ti64/xCu composites. Powder mixtures of Ti64/xCu were compacted in a die and then sintered at 1100 °C. Sintering kinetics indicate that densification is achieved by pore filling due to eutectic liquid formed by the reaction of Ti and Cu. The microstructure of the sintered samples is composed mainly of α-Ti and Ti_2Cu phases, but TixCuy intermetallics were also found. Microhardness is increased by the addition of Cu due to densification and the formation of harder phases such as $T_{i2}Cu$. However, the stiffness and compression strength are barely the same for all composites. The corrosion resistance is significantly improved by the addition of Cu. Finally, the material with 15 wt% of copper showed the best compromise.

Keywords: liquid-state sintering; Ti64 alloys; mechanical properties; corrosion; microstructure

Citation: Vergara-Hernández, H.J.; Olmos, L.; Solorio, V.M.; Bouvard, D.; Villalobos-Brito, J.; Chávez, J.; Jimenez, O. Powder Metallurgy Fabrication and Characterization of Ti6Al4V/xCu Alloys for Biomedical Applications. *Metals* **2023**, *13*, 888. https://doi.org/10.3390/met13050888

Academic Editor: Yadir Torres Hernández

Received: 31 March 2023
Revised: 20 April 2023
Accepted: 28 April 2023
Published: 4 May 2023

1. Introduction

Ti6Al4V (Ti64) alloy is the most-used material for biomedical implants such as dental and orthopedic prostheses, due to its good biocompatibility, high strength, excellent corrosion resistance under corporal fluids and good compatibility with living organisms [1,2]. Nevertheless, Ti64 alloy shows serious drawbacks such as poor wear resistance and low antibacterial activity, which may result in the early degradation of long-term prostheses [3]. To overcome these drawbacks, the addition of antibacterial metals such as silver and copper has been proposed [4–12]. It has been reported in [13,14] that a high level of antibacterial activity is reached with the addition of less than 5 wt% of Cu or Ag. Cu is preferentially used as an addition element into Ti alloys because it is a trace element in the human body, and it participates in different biological and physiological human functions [15]. Besides this, Cu can be eliminated from the human body through bile, and it shows a variety of beneficial effects on biological processes such as osteogenesis and angiogenesis [16]. Cu shows an antibacterial ability because bacteria are killed in contact with surfaces containing

Cu. In dry conditions this process can take a few minutes, while in wet conditions a longer time is needed [17,18]. For Ti–Cu alloys, it was demonstrated that Ti_2Cu intermetallic showed the best antibacterial effect [19], and it was also suggested that a small amount on the Ti_2Cu surface improved bacteria elimination [20]. Ti–Cu alloys have been fabricated by different methods, such as casting, powder metallurgy and additive manufacturing, as reported by Akbarpour et al. [21].

Although Ti64 is nowadays the most-used alloy for orthopedic and dental implant materials [22], only a few works have been devoted to analyzing the benefit of Cu addition [23–26]. Most of those works are devoted to the improvement of antibacterial and mechanical properties, including an increase in hardness [27,28]. The processing of Ti64/xCu alloys by the powder metallurgy route, comprising conventional pressing and sintering, has received less attention, as far as we know. The complexity of fabricating Ti64xCu alloys is due to the peritectic and eutectic reactions between Ti and Cu [29] that induce the formation of a liquid phase. Nevertheless, this phase could be beneficial for decreasing the sintering temperature in comparison to the one used for Ti64 alloy. Thus, this paper focuses on investigating the effect of Cu addition on the sintering behavior of TI64 powder and on characterizing the microstructure as well as the mechanical and corrosion properties of sintered composites.

2. Materials and Methods

An atomized prealloyed Ti64 powder with spherical particles smaller than 45 µm, produced by Raymor, Quebec, Canada, was mixed with spherical Cu particles with the same particle size distribution, provided by Sigma-Aldrich (St. Louis, MO, USA). The fraction of Cu particles was set between 0 and 20 wt%. Mixing was carried out in a Turbula for 30 min in dry conditions. Then, 1 wt% of polyvinyl alcohol (PVA) was added as a binder. Next, the mixture was poured into an 8 mm diameter stainless steel die and pressed up to 450 MPa using an Instron 1150 universal machine to obtain cylindrical compacts of either 4 or 10 mm height. Samples of 10 mm height were used for compressive tests. Each compact was sintered in a Linseis L75V (Selb, Germany) vertical dilatometer at 1100 °C with a dwell time of 5 min in argon. After sintering, the weight density of every sintered compact was calculated from mass and dimension measurements. The theoretical density of the composite materials chosen to compute the relative density was estimated by the rule of mixture. Sintered composites of 4 mm height were cut and subjected to metallographic preparation by grinding and polishing with SiC paper and alumina suspension to achieve a high-quality planar surface. The crystalline structure was assessed by X-ray diffraction (XRD) using an Emperyan Panalytical diffractometer with K-alpha copper radiation with an energy of 30 kV and 30 mA, with a 0.2 step size. A 1 s time step in a 2θ range of 30–80° was used in order to identify the constituent phases of sintered samples. Next, the polished surfaces were observed with a Jeol JSM 7600F (Tokyo, Japan) field-emission scanning electron microscope (FE-SEM) coupled with an energy-dispersive X-ray spectrometer (Bruker, XFlash 6 | 30, Billerica, MA, USA) for elemental and mapping analysis. Microhardness tests were performed on the polished surfaces with a Micro-Hardness tester, Mitutoyo MVK-HVL (Kawasaki, Japan), using a load of 200 gf and a dwell time of 15 s according to ASTM E384. In order to obtain representative values, 15 indentations were made for each sample, and the average value was calculated.

In order to evaluate the mechanical properties of the sintered samples, the bottom and top surfaces of each 10 mm high sample were polished, and simple compression tests were performed following ASTM D695-02 with an Instron 1150 universal mechanical testing machine at a strain rate of 0.5 $mm.min^{-1}$. The elastic modulus and yield strength were estimated from a stress–strain curve that was obtained from the load-displacement data provided by the machine. To calculate the stress, the surface area of the sample was corrected by assuming that the volume was constant during compression. The axial strain was calculated as the ratio of the real axial displacement (after machine stiffness correction) and the initial height of samples.

To evaluate the corrosion behavior of the sintered samples, electrochemical measurement was performed using a standard three-electrode system in a simulated body fluid Hank's solution provided by Sigma-Aldrich. A Corrtest 350CS (Wuhan, China) system was used for electrochemical tests with a saturated calomel electrode (SCE) as the reference electrode. The open circuit potential (OCP) was measured for 55 min after immersion in Hank's solution. To determine the corrosion rate, potentiodynamic polarization tests were performed in a potential range from −600 to 600 mV at a scanning rate of 1 mV/s, following ASTM G61. Besides this, electrochemical impedance spectroscopy (EIS) analysis was carried out applying 10 mV amplitude vs. OCP with a frequency range of 100 kHz up to 10 mHz. Nyquist and Bode diagrams were plotted in order to fit an Electrochemical Equivalent Circuit (EEC) to determine electrochemical parameters such as capacitance and resistance to charge transfer, as complementary analysis to the potentiodynamic tests.

3. Results and Discussion

3.1. Sintering

The axial strain variation during the sintering cycle for the Ti64 powder and the mixes with different Cu contents is shown in Figure 1a. All samples exhibit the same behavior, thermal expansion and then shrinkage (decreasing strain), which starts at 760 °C. Then, at 910 °C, the composites exhibit a small step (red rectangle in Figure 1a), which is more visible when the strain rate is plotted as a function of temperature (Figure 1b). This tempering of the shrinkage is likely generated by the beginning of the peritectic reaction between Ti and Cu at 925 °C, according to the phase diagram [29]. After this, the axial strain continues to decrease. This shrinkage is much faster for the samples containing 15 and 20 wt% of Cu, whereas those with 5 and 10 wt% of Cu show a much slower shrinkage rate: only a little faster than the rate for pure Ti64. This means that for low Cu content, shrinkage is mostly due to Ti64 particle sintering, while for high Cu content, the liquid phase resulting from the eutectic reaction between Ti and Cu [29] plays the prominent role.

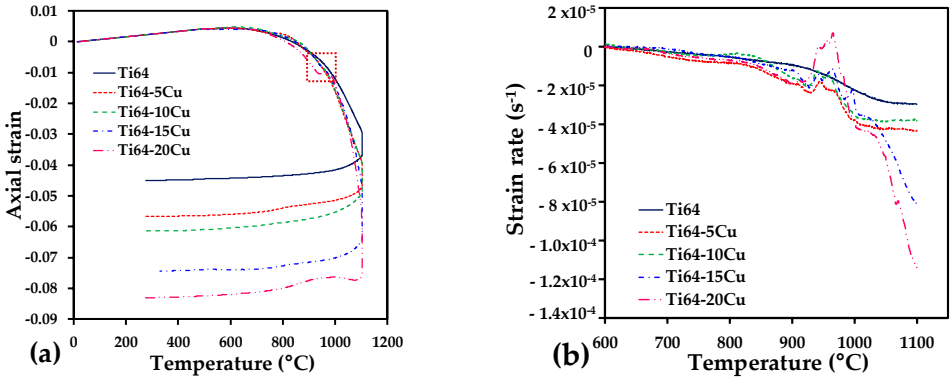

Figure 1. Axial strain as a function of temperature during the whole sintering cycle (**a**), and strain rate as a function of temperature during heating up to the sintering plateau (**b**).

The green and sintered densities of the samples are listed in Table 1. The green densities (D_0) of Ti64 and the composites are very close to each other. Ti64 and Cu powders have similar shapes and particle size distributions, but copper is softer than Ti64. We thus expected to find higher green densities for the composites. After sintering, the relative density (D_s) increases with increasing Cu fraction. The sample without Cu particles shows a low relative density, 78.8%, which is due to the low temperature used, 1100 °C, compared to usual sintering temperatures for this powder. The addition of 5 and 10 wt% of Cu increased the relative densities up to 81.3% and 83.4%. The addition of 15 wt% of Cu or more densifies the sample by over 90%. The maximum relative density is around 97% for 20 wt% of Cu. The final densification ratio defined as $((D_s - D_0)/D_0)$ is therefore three times larger for the sample with 20 wt% of Cu in comparison to that of the pure Ti64 sample.

Table 1. Green and sintered densities and densification ratio of all sintered samples.

Wt% of Cu	D_0	D_s	$(D_s - D_0)/D_0$
0	0.697	0.788	0.130
5	0.691	0.813	0.175
10	0.698	0.834	0.195
15	0.701	0.905	0.291
20	0.691	0.967	0.398

3.2. Microstructure Analysis

The microstructure of Ti64 and the composites was studied by SEM observation and EDS analysis of the polished surfaces of the samples.

3.2.1. SEM Observation

The microstructure of the Ti64 sample sintered at 1100 °C was analyzed in [5], in which large, cusped interparticle pores and small interparticle necks were seen. The addition of 5 and 10 wt% of Cu increased the relative densities up to 81.3% and 83.4%. Figure 2a,b shows smaller, more rounded pores and larger necks. The addition of 15 wt% of Cu or more densifies the sample by over 90%. The pores seem to be isolated, and most of them have a spherical shape (Figure 2c,d). Although it is likely that densification is mainly due to liquid formation and its flow through the interparticle pores of Ti64, the microstructures observed in Figure 2c,d are similar to those obtained by solidification. It can also be deduced that a strong solid-state diffusion of Cu to form intermetallics is achieved during the densification process. This is contrary to the observation of different systems that were sintered in a semi-solid state, in which the distribution of liquid is around the Ti64 particles either by means of a eutectic reaction [30] or the melting of one element [6]. Thus, the densification mechanism based on shrinkage during sintering and the microstructure obtained after sintering could be pore filling by eutectic liquid and growth of lamellae of Ti_2Cu during solidification of that liquid, which is increased by solid diffusion of Cu into the Ti64 matrix.

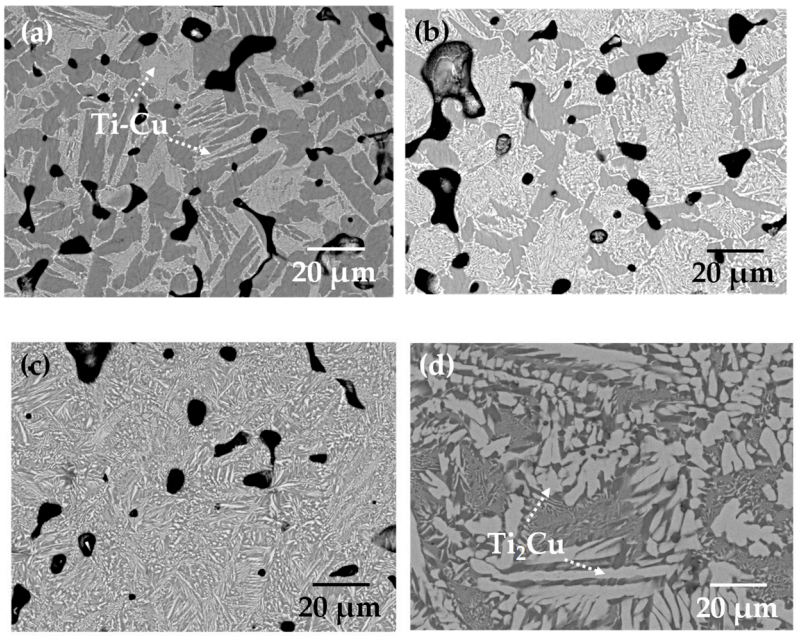

Figure 2. SEM micrographs of the samples sintered at 1100 °C: (**a**) Ti64-5Cu, (**b**) Ti64-10Cu, (**c**) Ti64-15Cu and (**d**) Ti64-20Cu.

The sample without Cu shows a classical α-β Ti phase microstructure, with predominant α-Ti and thin lamellae of β-Ti, as reported elsewhere [5]. The addition of Cu generates the formation of secondary phases inside the Ti64 particles that are mainly composed of Ti

and Cu. These components could be TiCu or Ti_2Cu intermetallics. Besides this, the lamellae of β-Ti are no longer detected; thus, the microstructure is formed by Ti–Cu intermetallics in a matrix of α-Ti (Figure 2d). As the quantity of Cu increases, the Ti–Cu phases are more homogeneously distributed inside the α-Ti matrix. It is interesting to note that for 20 wt% of Cu, the microstructure is composed of thick lamellae of Ti–Cu intermetallics embedded in an α-Ti matrix (Figure 2d).

Elemental mapping of the sample with 20 wt% of Cu illustrates that Cu is mainly located in the lamellae, although small quantities are detected over the whole surface (Figure 3a,c). In order to evaluate the composition of the phases, EDS analysis (spot mode) was performed at the three points indicated in Figure 3d. Point 1 is inside the Ti–Cu lamellae, and the atomic composition (Table 2) suggests that the Ti_2Cu phase is the main compound. This is consistent with the composition of the eutectic phase reported in the phase diagram [29]. The composition found at Point 2 shows a low quantity of Cu, which could indicate that solid-state diffusion of Cu is possibly occurring from the thick lamellae to the Ti64 matrix during solidification. Finally, the composition at Point 3 indicates mainly Ti64 alloy with a small increment in Al content. As Al is an α-Ti stabilizer, the β-Ti phase is no longer observed.

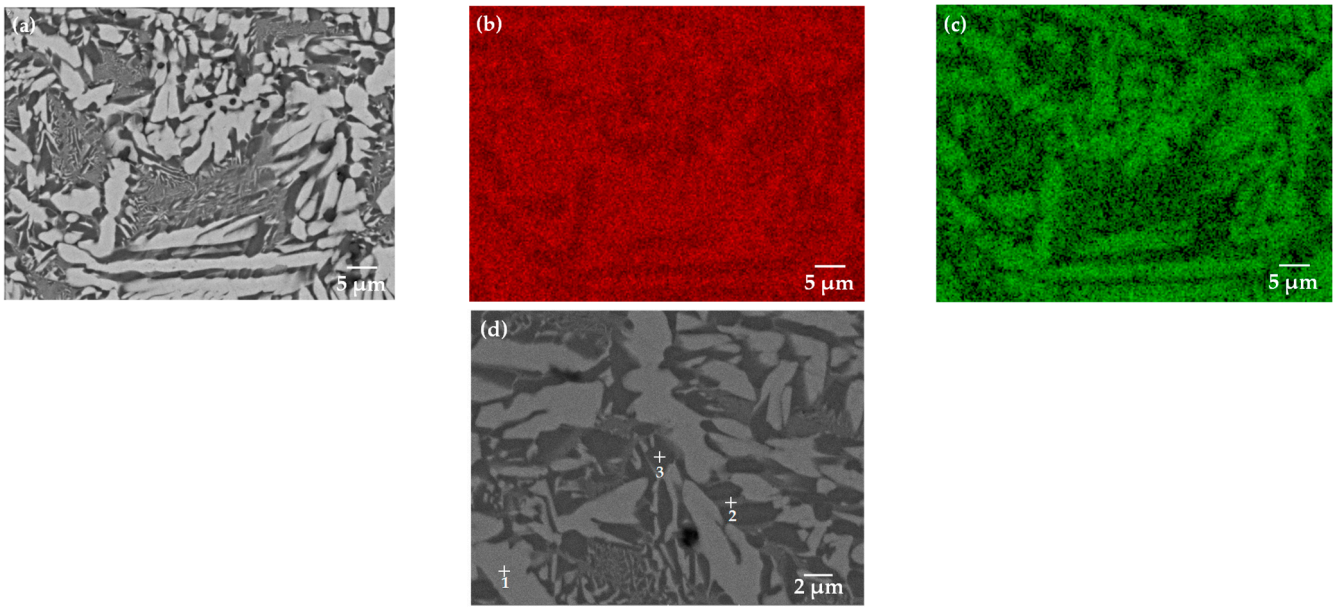

Figure 3. EDS elemental mapping of the composite containing 20% of Cu particles sintered at 1100 °C: (**a**) BSD image, (**b**) distribution of Ti, (**c**) distribution of Cu and (**d**) SEM image of the same composite indicating where (+) the EDS analysis (spot mode) was performed. Composition obtained from EDS is listed in Table 2, point 1, etc.

Table 2. EDS results of point analysis of Ti64–20 wt% Cu sample after sintering.

Element	At. %		
	Point 1	**Point 2**	**Point 3**
Ti	63.25	79.85	85.02
Cu	34.33	5.75	2.81
Al	2.41	10.28	7.99
V	0	4.09	4.17
Possible phase	Ti_2Cu	α-Ti	α-Ti

3.2.2. X-ray Diffraction Patterns

X-ray patterns of Ti64 and Ti64/xCu samples are plotted in Figure 4. The microstructure of Ti64 is mainly composed of hexagonal α-Ti with a small quantity of cubic β-Ti.

Addition of 5 wt% of Cu generates the formation of smaller quantities of Ti_xCu_y phases, which are formed during the peritectic and eutectic reactions occurring between Ti and Cu. Besides this, an V_5Al_8 intermetallic was found, which was probably formed because the Ti64 particles reduce their Ti quantity due to the formation of Ti_xCu_y phases. The formation and stabilization of Ti_2Cu, which increases with an increasing amount of Cu, is detected by an increment in the intensity of the main peak of this phase at 39.6°, as well as other characteristic peaks indicated in Figure 4. This confirms the phases detected by EDS in Figure 3d, which indicated two main phases of Ti_2Cu and α-Ti, similarly to Takada et al., who observed this in Ti/20Cu alloy fabricated by melting [31]. Evolution of the microstructure occurs because the quantity of Cu is sufficient to form eutectic liquid that can fully densify the sample and also solid-state diffusion during solidification. The formation of different Ti_xCu_y phases is possible during eutectic reaction since the quantities of Ti and Cu are not those reported in the equilibrium phase diagram [29]. It is also noticed that the main peak of the α-Ti phase at 40.4° is reduced as the wt% of Cu increases. This is different from other studies on Ti–Cu alloys fabricated by arc melting [32], vacuum sintering [13] and laser melting sintering of Ti64/6Cu [4], which report a predominant α-Ti phase for 10 wt% of Cu. This confirms that a significant space of the surface of the Ti64/20Cu sample is occupied by the Ti_2Cu phase, which is beneficial for antibacterial activity as reported elsewhere [20].

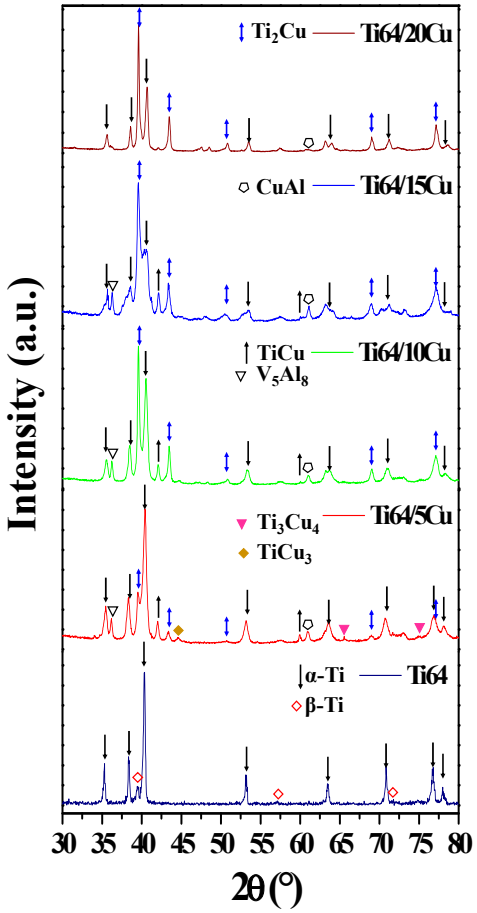

Figure 4. X-ray diffraction patterns of the samples with different wt% of Cu. The identified phases are indicated as follows: ↓ α-Ti, ◇ β-Ti, ▼ Ti_3Cu_4, ◆ $TiCu_3$, ▽ V_5Al_8, ↑ TiCu and ↕ Ti_2Cu.

3.3. Mechanical Properties

3.3.1. Microhardness

The microhardness of the samples is plotted in Figure 5a as a function of the wt% of Cu and in Figure 5b as a function of the remaining porosity after sintering. This shows a continuous increase with an increase in the amount of Cu and with the diminution of pores. The microhardness is 190 Hv for pure Ti64 alloy with a porosity of 0.21, and 420 Hv for the composite with 20 wt% of Cu and porosity of 0.03. The observed variation could be a direct effect of Cu resulting from the formation of Ti_2Cu, whose microhardness has been reported to be 800 Hv [33]. It could also be a consequence of the reduction of porosity caused by the presence of Cu. To evidence both effects of Cu, it can be reported that Ti64 powder sintered at 1260 °C with a porosity of 0.04 exhibited a hardness of 350 Hv [34], which is lower than that of Ti64/20wt% Cu with about the same relative density and is higher than that of Ti64 with a lower relative density. The microhardness value of the samples with 5 and 10 wt% of Cu agreed with those reported for Ti–Cu alloys fabricated by casting with the same quantity of Cu [35]. However, the values reported for Ti64/Cu alloys fabricated by SLM are slightly higher than those obtained here, likely because of internal stresses generated during processing [36].

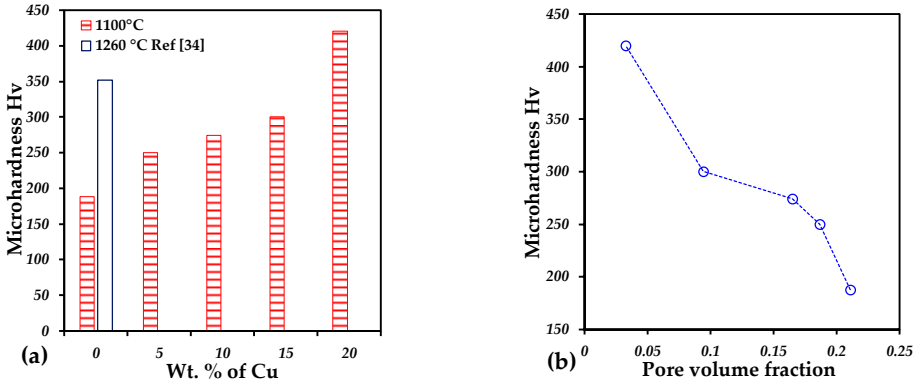

Figure 5. Microhardness as a function of (**a**) Cu content and (**b**) relative density of samples.

3.3.2. Compression Tests

The effect of Cu addition on compression behavior has been analyzed from the stress–strain curves shown in Figure 6. It is observed that strain before failure is significantly reduced for all composite samples except for the one with 10 wt% of Cu. Alshammari et al. [37] reported a reduction in compressive strain of 62% between Ti0.5Cu and Ti5Cu samples prepared by vacuum sintering, but the relative density was similar in their samples and lower Cu quantities were used.

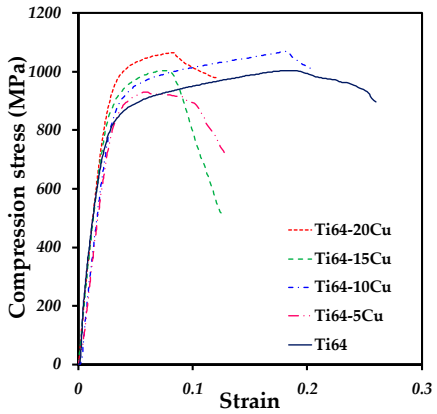

Figure 6. Stress–strain curves of compression tests for Ti64 and Ti64/xCu samples.

The Young's modulus is around 35 GPa for every sample. It is most likely that the slight variations found are within the inaccuracy range. These values are low in comparison with those evaluated by ultrasonic methods for Ti–Cu alloys fabricated by arc melting (110–135 GPa, depending on the Cu content) [35] and by SPS (greater than 110 GPa for different Cu contents) [38]. The Young's modulus of Ti–Cu alloys was also numerically estimated by Zhu et al. [33], taking into account the formation of Ti–Cu intermetallics. These authors obtained a value of 41 GPa for an alloy with 28 at.% of Cu, which corresponds to around 30 wt% of Cu. This reduction was mainly associated with the positive formation enthalpy of the Ti_3Cu phase.

The yield stress continuously increases from 590 to 781 MPa with increasing Cu content from 5 to 20 wt%, with the Ti64 sample showing a slightly lower value of 630 MPa. This increase is due to both the different microstructure, which is mainly composed of Ti_2Cu and α-Ti phases, and the lower porosity. These values are low compared to those reported for Ti–Cu alloys fabricated by vacuum sintering with amounts of Cu up to 10 wt% [39,40], but a close result was found for low Cu content by Alshammari et al. [37], who reported a yield stress of 627 MPa for a sintered Ti/5Cu alloy. This value is close to that obtained for our Ti64/5Cu sample. The ultimate strength is between 930 and 1100 MPa, without a clear trend. This suggests that the details of the microstructure do not play a major role in this property, which might be related to Ti64 interparticle necks formed during sintering before eutectic liquid appears. The values obtained are higher than that of 754 MPa reported by Alshammari et al. [37] for various Ti/Cu alloys, but much lower than that reported by Zhang et al. [39] for Ti/10Cu, of around 1800 MPa.

In addition, admissible strain, σ_y/E, has also been calculated for each sample. This increases slightly with increasing Cu wt% (Table 3). The admissible strain should be as high as possible for improved behavior of bone implants, as suggested in [41]. The values reported for compact and trabecular vertebrae bones are 17.5×10^{-3} and 20.8×10^{-3}, respectively [42], and are thus in the same range as those found here.

Table 3. Mechanical properties of Ti64 and Ti64/xCu composites.

Wt% Cu	E (GPa)	σ_y (MPa)	σ_u (MPa)	σ_y/E (10^{-3})
0	35.9	630	1004	17.5
5	32.5	590	930	18.1
10	33.3	684	1104	20.5
15	36.7	759	1000	20.7
20	37.5	781	1093	20.8

3.4. Corrosion Analysis

3.4.1. Potentiodynamic Analysis

In order to evaluate the corrosion behavior of Ti64/xCu samples, potentiodynamic tests were carried out, and polarization curves for the different samples sintered at 1100 °C are plotted in Figure 7. The corrosion potential E_{corr} and corrosion current density I_{corr} were estimated by using the Tafel extrapolation method, which is detailed elsewhere [43], and the values obtained are summarized in Table 4. It is observed that the addition of Cu improves corrosion resistance because E_{corr} increases towards electropositive values and I_{corr} decreases with increasing Cu content, caused by a reduction in the anodic reaction rate. E_{corr} clearly indicates that the addition of Cu improves the corrosion susceptibility. E_{corr} is −0.40 V for Ti64 and around −0.2 V for the Ti64/xCu composites. This indicates a reduction in the corrosion tendency, the highest value being −0.18 V, which was obtained with 5 wt% of Cu. A decrease in the E_{corr} value for Ti–Al–xCu alloys was also reported elsewhere, for Cu additions from 5 to 20 wt% [44]. In spite of the fact that Ti64 exhibits the more negative E_{corr} value, it is more positive than that reported for Ti64 samples fabricated by additive manufacturing under Hank's solution, which is −0.548 V [44]. There is no measurement reported for Ti64/xCu alloys under Hank's solution, but E_{corr} absolute values of Ti/5Cu and Ti/10Cu alloys are reported by Chen et al. [45], who obtained −0.662 and −0.598 V,

respectively, which are lower than those obtained in this work. The E_{corr} values reported for Ti64/xCu composites under artificial sea water were also more negative (−0.39 to −0.42 V) [26] than those found in this work, and the values reported for similar composites under simulated body fluid were similar to those here (−0.22 V) [7]. The positive effect of adding Cu could be due to the formation of Ti_2Cu and intermetallic phases formed during sintering that could promote a more stable passive layer than that formed by Ti, as described elsewhere [7,32].

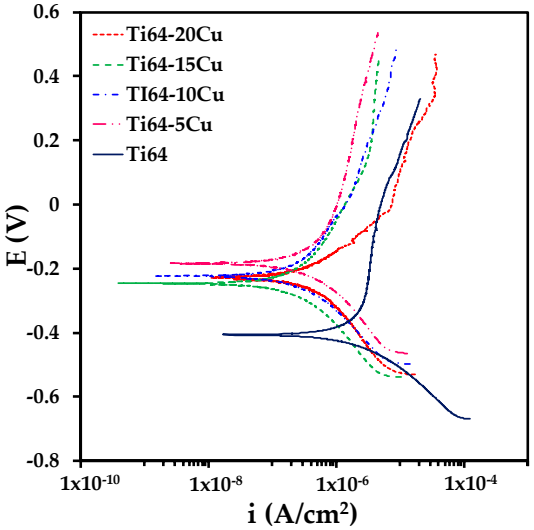

Figure 7. Polarization curves of composites under Hank's solution after sintering at 1100 °C.

Table 4. Corrosion parameters of Ti64 and Ti64/xCu samples sintered at 1100 °C.

Wt% Cu	I_{corr} (μA/cm^2)	E_{corr} (V)	V_{corr} (mm/year)
0	3.810	−0.407	0.079
5	0.855	−0.184	0.0143
10	0.375	−0.223	0.00625
15	0.276	−0.246	0.00461
20	0.512	−0.228	0.00829

I_{corr} shows a similar trend, as the highest value is found for Ti64, 3.81 μA-cm^{-2}. The composites show values lower than 1 μA-cm^{-2}, with a minimum of 0.276 μA-cm^{-2} for the Ti64/15Cu sample. The value obtained for Ti64 is much higher than those reported for additively manufactured Ti64 (0.008 μA-cm^{-2}) under Hank's solution [45], which is probably due to the high porosity of the sample sintered at 1100 °C. However, the values obtained for the Ti64/xCu samples are lower than those reported for Ti–Cu alloys fabricated by melting [45–47] under Hank's solution or by sintering under NaCl [13], in spite of the remaining porosity. I_{corr} is linked to the corrosion rate (V_{corr}) by means of Faraday's law [47]:

$$V_{corr} = \frac{MI_{corr}}{nF\rho_m} \quad (1)$$

where M is the molar mass of the alloy, n is the charge of the metal ions, F is the Faraday constant and ρ_m is the density of the alloy. The corrosion rates for each sample were calculated and are listed in Table 4. The addition of Cu results in a strong reduction in the corrosion rate. It is found that V_{corr} is 17 times lower with 15 wt% of Cu with respect to pure Ti64. This value is also 10 times lower than that reported for Ti64/xCu composites under sea water [26]. Although E_{corr} indicates corrosion tendency, a more appropriate parameter to measure corrosion would be I_{corr} or V_{corr}, which confirm that corrosion is improved by the addition of Cu. The optimum behavior is obtained with the Ti64/15Cu

sample, which also shows a stable passivation film at a potential of 0.1 V, similar to that reported for Ti–Cu alloys [7].

3.4.2. Electrochemical Impedance Spectroscopy Analysis

In order to evaluate the corrosion mechanism of the Ti64/xCu samples, EIS tests were carried out for the different samples sintered at 1100 °C in Hank's solution, and the EEC were fitted as presented in Figure 8. In addition, the EIS parameters obtained from the EEC are listed in Table 5. Figure 8a corresponds to a Nyquist plot, in which real impedance (Z′) and imaginary impedance (Z″) are observed. These have a tendency to form a linear behavior of about 45°, characteristic of a mass transfer of chemical species from the Hank's solution into the sample. This behavior is observed in all Ti64/xCu samples. However, it is important to observe that the Ti64 condition showed a lower impedance related to a higher susceptibility to corrode in the evaluated media. Otherwise, the samples which contain Cu increased their impedance values, indicating a higher resistance to corrosion in general terms. This behavior is corroborated in Figure 8b, a Bode vs. frequency plot, which represents the impedance magnitude |Z| as a function of frequency, which is higher as Cu content increases. However, Ti64/20Cu showed a slight decrease in its values, which could be related to the presence of intermetallic composites such as Ti_2Cu, which reduce corrosion resistance by a lower solid solution of Cu content. Figure 8c shows a Bode vs. phase angle plot, which shows a maximum peak of phase angle near to −70 degrees at lower frequencies for the Ti64/xCu samples. However, the Ti64 condition showed a lower phase angle peak of about −40 degrees, which represents different processes that are analyzed by an EEC (Figure 8d). The behavior observed in the EIS analysis are in concordance with the corrosion parameter obtained by potentiodynamic tests.

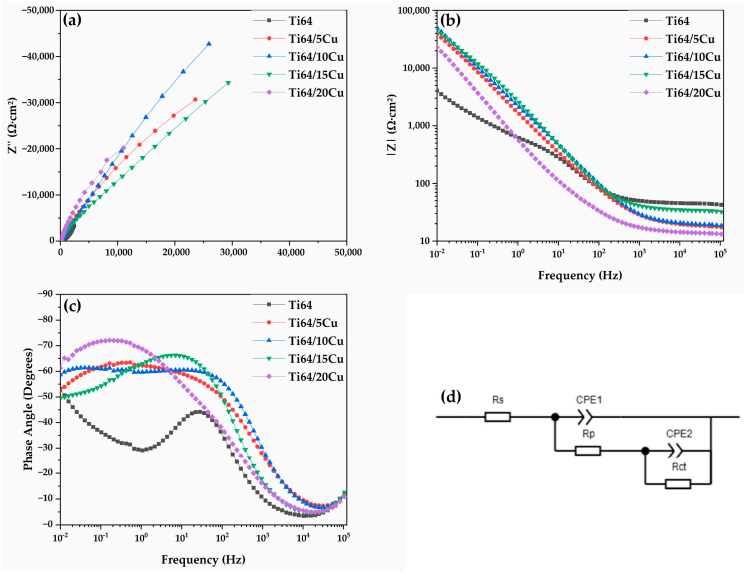

Figure 8. (**a**) Nyquist plot, (**b**) Bode–frequency plot, (**c**) Bode–phase angle plot and (**d**) electrochemical equivalent circuit of composites under Hank's solution after sintering at 1100 °C.

To quantify the effect of Cu content in the Ti64 samples, an EEC model was proposed and showed accurate fitting between the experimental and theoretical data, which are composed of the following elements: a resistive element that represents the solution resistance between the working electrode and the reference electrode (RS); and porous resistance (Rp) and its corresponding constant phase element (CPE1). However, in parallel to those elements are proposed a charge transfer in the electrode/electrolyte interface (RCT) element and a capacitive element that was replaced by a constant phase element (CPE2) which is generally used to adjust stabilization times due to the effect of rough or porous surfaces [48–50]. From these parameters, it is important to analyze the Rp

values of the different samples evaluated; the Ti64 condition obtained an Rp value of about 674 Ω·cm^2, which reduces considerably as Cu content increases up to 22 Ω·cm^2 for Ti64/20Cu. This Rp reduction is related to the increase in relative density (Ds) as Cu content increases; as observed in the micrographs in Figure 2, the porosity is lower due to the higher densification effect of Cu. On the other hand, the Rct values represent a charge transfer resistance mechanism which is directly related to the susceptibility to corrosion in the evaluated samples. A similar behavior is observed in the V_{corr} values obtained in potentiodynamic tests; the Ti64 sample gave a value of 21,097 Ω·cm^2, which increased as Cu content increased. However, the same behavior is observed for Ti64/20Cu: a slight reduction in Rp values, as observed in V_{corr}, which was abovementioned. Another important factor to take into account for the increase in Rct values is related to the active area of the samples. The Ti64 condition showed a lower densification ratio, and therefore a higher electrochemical active area, which increases the rate of anodic reaction. Otherwise, the Ti64/15Cu and Ti64/20Cu showed a better performance of corrosion behavior with a reduction in the electrochemical active area, which reduces the rate of anodic reaction, and this is related to a higher densification ratio as presented in the previous section [51]. This effect was studied by Fangxia Xie et al. [52], and they concluded that an increment of pores in the sample means that it is more susceptible to corrosion attack.

Table 5. Electrochemical parameters obtained from electrochemical equivalent circuit of Ti64 and Ti64/xCu samples sintered at 1100 °C evaluated under Hank's solution.

Wt% Cu	Rs (Ω·cm^2)	CPE1 (F s$^{\alpha-1}$ cm^{-2})	N	Rp (Ω·cm^2)	CPE2 (F s$^{\alpha-1}$ cm^{-2})	n	R_{ct} (Ω·cm^2)
0	44.41	0.000146	0.7477	674.77	0.001310	0.6424	21,097
5	29.25	0.000124	0.6110	199.98	0.000641	0.7051	52,120
10	17.12	0.000105	0.6429	56.64	0.000249	0.8141	70,253
15	11.67	0.000561	0.4255	26.82	0.000601	0.8270	122,103
20	14.05	0.000223	0.7779	22.03	0.000306	0.7703	85,505

However, additional tests of cytotoxicity should be made to determine the concentration of Cu ions, since it has been demonstrated that high Cu ion concentration inhibits cell proliferation and could have a toxic response in humans [53,54].

4. Conclusions

Ti64/xCu composites have been successfully fabricated by conventional powder metallurgy. Sintering is driven by a liquid phase due to the eutectic reaction occurring during the heating stage. The shrinkage kinetics indicate that adding 15 wt% of Cu strongly improves densification, which is assumed to be achieved by pore filling by eutectic liquid and solid diffusion of Cu into the Ti64 matrix during solidification. The maximum relative density reached was 97% for 20 wt% of Cu after sintering at 1100 °C.

The final microstructure of the composites is mainly composed of two phases, α-Ti and Ti_2Cu, although small amounts of Ti–Cu intermetallics with different compositions are also present. It was also assessed that Cu diffusion forms thin lamellae of Ti_2Cu that grow and form thicker lamellae when the quantity of Cu is 20 wt%.

The microhardness was improved by the addition of Cu in comparison with that of Ti64 sintered at the same temperature, which is attributed to the higher relative density and the formation of the Ti_2Cu phase. On the contrary, the mechanical strength obtained from compression tests does not show an increase with respect to the Ti64 sample, because the mechanical response is governed by the size of necks formed during sintering.

Corrosion under Hank's solution is improved by Cu addition because of the formation of a stable Ti_2Cu layer. It can be concluded that the material with 15 wt% of Cu shows the best compromise between corrosion and mechanical properties, although its relative density is only 90%.

Author Contributions: H.J.V.-H.: conceptualization, methodology and project administration. L.O.: writing—original draft and formal analysis. V.M.S.: methodology. D.B.: writing—review and editing. J.V.-B.: corrosion test and analysis. J.C.: experimentation and formal analysis. O.J.: validation and visualization. All authors have read and agreed to the published version of the manuscript.

Funding: This work was supported by the National Council for Science and Technology CONACYT (Victor Manuel Solorio PhD scholarship 760947). The authors would like to thank the CIC of the UMSNH and the National Laboratory SEDEAM-CONACYT for the financial support and facilities provided for the development of this study. The APC was funded by Tecnológico Nacional de México/Instituto Tecnológico de Morelia via H.J. Vergara-Hernández.

Data Availability Statement: The raw/processed data required to reproduce these findings cannot be shared at this time as the data also form part of an ongoing study.

Conflicts of Interest: The authors declare that they have no known competing financial interest or personal relationships that could have appeared to influence the work reported in this paper.

References

1. Oshida, Y. *Bioscience and Bioengineering of Titanium Materials*; Elsevier: Amsterdam, The Netherlands, 2010; ISBN 0080467199.
2. Yuan, Z.; He, Y.; Lin, C.; Liu, P.; Cai, K. Antibacterial Surface Design of Biomedical Titanium Materials for Orthopedic Applications. *J. Mater. Sci. Technol.* **2021**, *78*, 51–67. [CrossRef]
3. Xu, X.; Lu, Y.; Li, S.; Guo, S.; He, M.; Luo, K.; Lin, J. Copper-Modified Ti6Al4V Alloy Fabricated by Selective Laser Melting with pro-Angiogenic and Anti-Inflammatory Properties for Potential Guided Bone Regeneration Applications. *Mater. Sci. Eng. C* **2018**, *90*, 198–210. [CrossRef]
4. Luo, J.; Guo, S.; Lu, Y.; Xu, X.; Zhao, C.; Wu, S.; Lin, J. Cytocompatibility of Cu-Bearing Ti6Al4V Alloys Manufactured by Selective Laser Melting. *Mater. Charact.* **2018**, *143*, 127–136. [CrossRef]
5. Solorio, V.M.; Vergara-Hernández, H.J.; Olmos, L.; Bouvard, D.; Chávez, J.; Jimenez, O.; Camacho, N. Effect of the Ag Addition on the Compressibility, Sintering and Properties of Ti6Al4V/XAg Composites Processed by Powder Metallurgy. *J. Alloys Compd.* **2022**, *890*, 161813. [CrossRef]
6. Xin, C.; Wang, N.; Chen, Y.; He, B.; Zhao, Q.; Chen, L.; Tang, Y.; Luo, B.; Zhao, Y.; Yang, X. Biological Corrosion Behaviour and Antibacterial Properties of Ti-Cu Alloy with Different Ti_2Cu Morphologies for Dental Applications. *Mater. Des.* **2022**, *215*, 110540. [CrossRef]
7. Zhang, E.; Li, F.; Wang, H.; Liu, J.; Wang, C.; Li, M.; Yang, K. A New Antibacterial Titanium–Copper Sintered Alloy: Preparation and Antibacterial Property. *Mater. Sci. Eng. C* **2013**, *33*, 4280–4287. [CrossRef] [PubMed]
8. Xie, Y.; Lu, M.; Mao, X.; Yu, H.; Zhang, E. Enhancing the Antibacterial Properties and Biocompatibility of Ti-Cu Alloy by Roughening and Anodic Oxidation. *Metals* **2022**, *12*, 1726. [CrossRef]
9. Xie, Y.; Lu, M.; Cui, S.; Yu, H.; Wang, L.; Ke, H.; Zhang, E. Construction of a rough surface with submicron Ti_2Cu particle on Ti-Cu alloy and its effect on the antibacterial properties and cell biocompatibility. *Metals* **2022**, *12*, 1008. [CrossRef]
10. Wu, Y.; Zhou, H.; Zeng, Y.; Xie, H.; Ma, D.; Wang, Z.; Liang, H. Recent advances in copper-doped titanium implants. *Materials* **2022**, *15*, 2342. [CrossRef]
11. Yeshanew, S.K.; Bai, C.; Jia, Q.; Xi, T.; Zhang, Z.; Li, D.; Xia, Z.; Yang, R.; Yang, K. Microstructure Evolution and Deformation Mechanisms of As-Cast Antibacterial Ti6Al4V-5Cu Alloy for Isothermal Forging Process. *Materials* **2022**, *15*, 3349. [CrossRef] [PubMed]
12. Dyal Ukabhai, K.; Curle, U.A.; Masia, N.D.E.; Smit, M.; Mwamba, I.A.; Norgren, S.; Öhman-Mägi, C.; Hashe, N.G.; Cornish, L.A. Formation of Ti_2Cu in Ti-Cu alloys. *J. Phase. Equilibria Diffus.* **2022**, *43*, 332–344. [CrossRef]
13. Lei, Z.; Zhang, H.; Zhang, E.; You, J.; Ma, X.; Bai, X. Antibacterial Activities and Biocompatibilities of Ti-Ag Alloys Prepared by Spark Plasma Sintering and Acid Etching. *Mater. Sci. Eng. C* **2018**, *92*, 121–131. [CrossRef] [PubMed]
14. Wang, P.; Yuan, Y.; Xu, K.; Zhong, H.; Yang, Y.; Jin, S.; Yang, K.; Qi, X. Biological Applications of Copper-Containing Materials. *Bioact. Mater.* **2021**, *6*, 916–927. [CrossRef]
15. Jacobs, A.; Renaudin, G.; Forestier, C.; Nedelec, J.-M.; Descamps, S. Biological Properties of Copper-Doped Biomaterials for Orthopedic Applications: A Review of Antibacterial, Angiogenic and Osteogenic Aspects. *Acta. Biomater.* **2020**, *117*, 21–39. [CrossRef]
16. Santo, C.E.; Lam, E.W.; Elowsky, C.G.; Quaranta, D.; Domaille, D.W.; Chang, C.J.; Grass, G. Bacterial Killing by Dry Metallic Copper Surfaces. *Appl. Environ. Microbiol.* **2011**, *77*, 794–802. [CrossRef] [PubMed]
17. Andersen, O.Z.; Offermanns, V.; Sillassen, M.; Almtoft, K.P.; Andersen, I.H.; Sørensen, S.; Jeppesen, C.S.; Kraft, D.C.E.; Bøttiger, J.; Rasse, M. Accelerated Bone Ingrowth by Local Delivery of Strontium from Surface Functionalized Titanium Implants. *Biomaterials* **2013**, *34*, 5883–5890. [CrossRef]
18. Mahmoudi, P.; Akbarpour, M.R.; Lakeh, H.B.; Jing, F.; Hadidi, M.R.; Akhavan, B. Antibacterial Ti–Cu implants: A critical review on mechanisms of action. *Mater. Today Bio* **2022**, *17*, 100447. [CrossRef]

19. Zhang, E.; Wang, X.; Chen, M.; Hou, B. Effect of the Existing Form of Cu Element on the Mechanical Properties, Bio-Corrosion and Antibacterial Properties of Ti-Cu Alloys for Biomedical Application. *Mater. Sci. Eng. C* **2016**, *69*, 1210–1221. [CrossRef]
20. Ng, H.P.; Nandwana, P.; Devaraj, A.; Semblanet, M.; Nag, S.; Nakashima, P.N.H.; Meher, S.; Bettles, C.J.; Gibson, M.A.; Fraser, H.L. Conjugated Precipitation of Twin-Related α and Ti_2Cu Phases in a Ti–25V–3Cu Alloy. *Acta Mater.* **2015**, *84*, 457–471. [CrossRef]
21. Akbarpour, M.R.; Mirabad, H.M.; Hemmati, A.; Kim, H.S. Processing and Microstructure of Ti-Cu Binary Alloys: A Comprehensive Review. *Prog. Mater. Sci.* **2022**, *127*, 100933. [CrossRef]
22. Kaur, M.; Singh, K. Review on Titanium and Titanium Based Alloys as Biomaterials for Orthopaedic Applications. *Mater. Sci. Eng. C* **2019**, *102*, 844–862. [CrossRef] [PubMed]
23. Ren, L.; Ma, Z.; Li, M.; Zhang, Y.; Liu, W.; Liao, Z.; Yang, K. Antibacterial Properties of Ti–6Al–4V–XCu Alloys. *J. Mater. Sci. Technol.* **2014**, *30*, 699–705. [CrossRef]
24. Peng, C.; Zhang, S.; Sun, Z.; Ren, L.; Yang, K. Effect of Annealing Temperature on Mechanical and Antibacterial Properties of Cu-Bearing Titanium Alloy and Its Preliminary Study of Antibacterial Mechanism. *Mater. Sci. Eng. C* **2018**, *93*, 495–504. [CrossRef]
25. Yang, J.; Qin, H.; Chai, Y.; Chen, Y.; Yang, K.; Qin, M.; Zhang, Y.; Xia, H.; Ren, L.; Yu, B. Molecular Mechanisms of Osteogenesis and Antibacterial Activity of Cu-Bearing Ti Alloy in a Bone Defect Model with Infection In Vivo. *J. Orthop. Transl.* **2021**, *27*, 77–89. [CrossRef]
26. Guo, S.; Lu, Y.; Wu, S.; Liu, L.; He, M.; Zhao, C.; Gan, Y.; Lin, J.; Luo, J.; Xu, X. Preliminary Study on the Corrosion Resistance, Antibacterial Activity and Cytotoxicity of Selective-Laser-Melted Ti6Al4V-XCu Alloys. *Mater. Sci. Eng. C* **2017**, *72*, 631–640. [CrossRef]
27. Machio, C.; Mathabathe, M.N.; Bolokang, A.S. A comparison of the microstructures, thermal and mechanical properties of pressed and sintered Ti–Cu, Ti–Ni and Ti–Cu–Ni alloys intended for dental applications. *J. Alloys Compd.* **2020**, *848*, 156494. [CrossRef]
28. Yu, F.; Wang, H.; Yuan, G.; Shu, X. Effect of Cu Content on Wear Resistance and Mechanical Behavior of Ti–Cu Binary Alloys. *Appl. Phys. A* **2017**, *123*, 278. [CrossRef]
29. Murray, J.L. The Cu−Ti (Copper-Titanium) System. *Bull. Alloy Phase Diagr.* **1983**, *4*, 81–95. [CrossRef]
30. Mihalcea, E.; Hernández, H.V.; Olmos, L.; Jimenez, O. Semi-Solid Sintering of Ti6Al4V/CoCrMo Composites for Biomedical Applications. *Mater. Res.* **2019**, *22*. [CrossRef]
31. Takada, Y.; Nakajima, H.; Okuno, O.; Okabe, T. Microstructure and Corrosion Behavior of Binary Titanium Alloys with Beta-Stabilizing Elements. *Dent. Mater. J.* **2001**, *20*, 34–52. [CrossRef] [PubMed]
32. Yi, C.; Ke, Z.; Zhang, L.; Tan, J.; Jiang, Y.; He, Z. Antibacterial Ti-Cu Alloy with Enhanced Mechanical Properties as Implant Applications. *Mater. Res. Express* **2020**, *7*, 105404. [CrossRef]
33. Zhu, Y.D.; Yan, M.F.; Zhang, Y.X.; Zhang, C.S. First-Principles Investigation of Structural, Mechanical and Electronic Properties for Cu–Ti Intermetallics. *Comput. Mater. Sci.* **2016**, *123*, 70–78. [CrossRef]
34. Cabezas-Villa, J.L.; Lemus-Ruiz, J.; Bouvard, D.; Jiménez, O.; Vergara-Hernández, H.J.; Olmos, L. Sintering Study of Ti6Al4V Powders with Different Particle Sizes and Their Mechanical Properties. *Int. J. Miner. Metall. Mater.* **2018**, *25*, 1389–1401. [CrossRef]
35. Kikuchi, M.; Takada, Y.; Kiyosue, S.; Yoda, M.; Woldu, M.; Cai, Z.; Okuno, O.; Okabe, T. Mechanical Properties and Microstructures of Cast Ti–Cu Alloys. *Dent. Mater.* **2003**, *19*, 174–181. [CrossRef] [PubMed]
36. Erinosho, M.F.; Akinlabi, E.T.; Pityana, S.; Owolabi, G. Laser Surface Modification of Ti6Al4V-Cu for Improved Microhardness and Wear Resistance Properties. *Mater. Res.* **2017**, *20*, 1143–1152. [CrossRef]
37. Alshammari, Y.; Yang, F.; Bolzoni, L. Low-Cost Powder Metallurgy Ti-Cu Alloys as a Potential Antibacterial Material. *J. Mech. Behav. Biomed. Mater.* **2019**, *95*, 232–239. [CrossRef] [PubMed]
38. Dong, R.; Zhu, W.; Zhao, C.; Zhang, Y.; Ren, F. Microstructure, Mechanical Properties, and Sliding Wear Behavior of Spark Plasma Sintered Ti-Cu Alloys. *Metall. Mater. Trans. A* **2018**, *49*, 6147–6160. [CrossRef]
39. Zhang, E.; Li, S.; Ren, J.; Zhang, L.; Han, Y. Effect of Extrusion Processing on the Microstructure, Mechanical Properties, Biocorrosion Properties and Antibacterial Properties of Ti-Cu Sintered Alloys. *Mater. Sci. Eng. C* **2016**, *69*, 760–768. [CrossRef]
40. Liu, J.; Li, F.; Liu, C.; Wang, H.; Ren, B.; Yang, K.; Zhang, E. Effect of Cu Content on the Antibacterial Activity of Titanium–Copper Sintered Alloys. *Mater. Sci. Eng. C* **2014**, *35*, 392–400. [CrossRef]
41. Song, Y.; Xu, D.S.; Yang, R.; Li, D.; Wu, W.T.; Guo, Z.X. Theoretical Study of the Effects of Alloying Elements on the Strength and Modulus of β-Type Bio-Titanium Alloys. *Mater. Sci. Eng. A* **1999**, *260*, 269–274. [CrossRef]
42. Wang, X.; Xu, S.; Zhou, S.; Xu, W.; Leary, M.; Choong, P.; Qian, M.; Brandt, M.; Xie, Y.M. Topological Design and Additive Manufacturing of Porous Metals for Bone Scaffolds and Orthopaedic Implants: A Review. *Biomaterials* **2016**, *83*, 127–141. [CrossRef]
43. Li, D.; Lin, C.; Batchelor-McAuley, C.; Chen, L.; Compton, R.G. Tafel Analysis in Practice. *J. Electroanal. Chem.* **2018**, *826*, 117–124. [CrossRef]
44. Sherif, E.S.M.; Abdo, H.S.; Latief, F.H.; Alharthi, N.H.; El Abedin, S.Z. Fabrication of Ti–Al–Cu new alloys by inductive sintering, characterization, and corrosion evaluation. *J. Mater. Res. Technol.* **2019**, *8*, 4302–4311. [CrossRef]
45. Chen, L.-Y.; Zhang, H.-Y.; Zheng, C.; Yang, H.-Y.; Qin, P.; Zhao, C.; Lu, S.; Liang, S.-X.; Chai, L.; Zhang, L.-C. Corrosion Behavior and Characteristics of Passive Films of Laser Powder Bed Fusion Produced Ti–6Al–4V in Dynamic Hank's Solution. *Mater. Des.* **2021**, *208*, 109907. [CrossRef]
46. Osório, W.R.; Freire, C.M.; Caram, R.; Garcia, A. The Role of Cu-Based Intermetallics on the Pitting Corrosion Behavior of Sn–Cu, Ti–Cu and Al–Cu Alloys. *Electrochim. Acta* **2012**, *77*, 189–197. [CrossRef]

47. Bao, M.; Wang, X.; Yang, L.; Qin, G.; Zhang, E. Tribocorrosion Behavior of Ti–Cu Alloy in Hank's Solution for Biomedical Application. *J. Bio- Tribo-Corros.* **2018**, *4*, 29. [CrossRef]
48. Kramer, M.; Tomkiewicz, M. Porous Electrodes: I. Numerical Simulation Using Random Network and Single-Pore Models. *J. Electrochem. Soc.* **1984**, *131*, 1283. [CrossRef]
49. Navarro-Flores, E.; Chong, Z.; Omanovic, S. Characterization of Ni, NiMo, NiW and NiFe electroactive coatings as electrocatalysts for hydrogen evolution in an acidic medium. *J. Mol. Catal. A Chem.* **2005**, *226*, 179–197. [CrossRef]
50. Navarro-Flores, E.; Omanovic, S. Hydrogen evolution on nickel incorporated in three-dimensional conducting polymer layers. *J. Mol. Catal. A Chem.* **2005**, *242*, 182–194. [CrossRef]
51. Alves, A.C.; Sendão, I.; Ariza, E.; Toptan, F.; Ponthiaux, P.; Pinto, A.M.P. Corrosion behaviour of porous Ti intended for biomedical applications. *J. Porous Mater.* **2016**, *23*, 1261–1268. [CrossRef]
52. Xie, F.; He, X.; Cao, S.; Mei, M.; Qu, X. Influence of pore characteristics on microstructure, mechanical properties and corrosion resistance of selective laser sintered porous Ti–Mo alloys for biomedical applications. *Electrochim. Acta* **2013**, *105*, 121–129. [CrossRef]
53. O'Hern, C.I.; Djoko, K.Y. Copper cytotoxicity: Cellular casualties of noncognate coordination chemistry. *mBio* **2022**, *13*, e00434-22. [CrossRef] [PubMed]
54. Cortizo, M.C.; Lorenzo de Mele, M.F. Cytotoxicity of copper ions released from metal: Variation with the exposure period and concentration gradients. *Biol. Trace. Elem. Res.* **2004**, *102*, 129–141. [CrossRef] [PubMed]